

Contents lists available at ScienceDirect

International Journal of Solids and Structures

journal homepage: www.elsevier.com/locate/ijsolstr



Actuation-Induced stable crack growth in near-equiatomic nickeltitanium shape memory alloys: Experimental and numerical analysis



S. Jape ^a, B. Young ^b, B. Haghgouyan ^b, C. Hayrettin ^b, T. Baxevanis ^c, D.C. Lagoudas ^{a,b}, I. Karaman ^{b,*}

- ^a Department of Aerospace Engineering, Texas A&M University, College Station 77843 TX, USA
- ^b Department of Materials Science and Engineering, Texas A&M University, College Station 77843 TX, USA
- ^c Department of Mechanical Engineering, University of Houston, Houston 77004 TX, USA

ARTICLE INFO

Article history:
Received 10 December 2019
Received in revised form 21 July 2020
Accepted 28 September 2020
Available online 7 October 2020

Keywords: Shape memory alloys NiTi Actuation Crack growth Fracture

ABSTRACT

Shape Memory Alloy (SMA) actuation technology requires a thorough understanding of the failure response of these alloys under loading that involves thermal variations, termed "actuation" loading. In this paper, the experimental observation of stable crack growth in SMA compact tension specimens during temperature changes under constant bias loads is reported for the first time. The intrinsic damage mechanisms that promote crack advance are those reported in literature for nominally isothermal overload fracture, *i.e.*, cleavage assisted by ductile void growth. Moreover, a numerical analysis is employed, and the resulting simulations are compared with the experimental data with the purpose of building confidence in the insight provided on the role of extrinsic mechanisms that further promote or impede crack advance. It is concluded that phase transformation plays a dual role on the crack growth kinetics by promoting crack growth when occurring in a fan in front of the crack tip and providing the toughness enhancement that results in stable crack growth when left in the wake of the advancing crack. While the latter is well known as transformation-induced toughness enhancement, the former has just been recently observed experimentally and is characteristic of SMAs subjected to actuation loading conditions.

1. Introduction

Shape Memory Alloys (SMAs) are a class of active materials with the ability to undergo repeatable reversible macroscopic shape change when subjected to thermal and/or mechanical stimuli, due to solid-to-solid diffusionless phase transformation (Lagoudas, 2008). In these materials, transformation between the parent austenite phase (high symmetry, stable at high temperature) and product martensite phase (low symmetry, stable at low temperature) at the microstructural level gives rise to the unique macroscopic properties of superelasticity (or pseudoelasticity) and shape memory effect. In the former, macroscopic shape change is typically accomplished by isothermal mechanical loading at high temperature, whereas in the latter, shape change generally results from nominally isobaric temperature change (Otsuka and Wayman, 1999; Wayman et al., 1972; Miyazaki et al., 1986; Shaw and Kyriakides, 1995). When SMA is subjected to a constant load followed by cyclic temperature variation, the resulting shape change can be utilized to perform mechanical work and the SMA

can be effectively used as a solid-state actuator (Kockar et al., 2008; Atli et al., 2011; Karakoc et al., 2019; Benafan et al., 2014; Nematollahi et al., 2018; Karakalas et al., 2019a, 2019b). Of the many SMA compositions, nickel-titanium (NiTi) is the most commonly known and commercially available alloy system and is used in a wide range of engineering applications (e.g., biomedical, automotive, aerospace) due to its superior mechanical properties, excellent corrosion resistance, and biocompatibility (Hartl and Lagoudas, 2007; El Feninat et al., 2002; Nematollahi et al., 2019; Jiang et al., 2016; Mohajeri et al., 2020; Jahadakbar et al., 2020). The most extensive applications of NiTi SMAs since their discovery have been in the biomedical industry as cardiovascular stents, and orthodontic and orthopedic implants. Recently, however, there has been an increasing interest in SMAs as solid-state actuators. Solidstate actuators are preferable to conventional actuators (e.g., hydraulic or electromagnetic) in applications where reduction in weight, volume or complexity is desired (Hartl and Lagoudas, 2007; Iwanaga et al., 1988). Moreover, due to their ability to exhibit reversible and repetitive phase transformation under high stress levels (up to 500 MPa) and with large recoverable strains, SMA actuators have actuation energy density comparable to or higher than that in existing actuation systems.

^{*} Corresponding author.

E-mail address: ikaraman@tamu.edu (I. Karaman).

Despite several demonstrations and flight tests of SMA actuators, a lack of systematic understanding of SMA actuation fatigue and fracture response has relegated these actuators to noncritical/non-structural applications with severe overdesigning. Thus, to utilize SMA actuators in practical engineering applications, especially where their failure can cause property damage or casualties, the fatigue and fracture properties of these materials under actuation loading paths, *i.e.*, under constant mechanical load and thermal variations, must be thoroughly understood. It is therefore critical to establish a fundamental scientific understanding and generate sufficient experimental data regarding the actuation fatigue and fracture response of SMAs (Hartl and Lagoudas, 2007).

The available literature on the fracture response of NiTi SMAs has been entirely within the purview of fracture under isothermal mechanical loading (Baxevanis and Lagoudas, 2015). Stressinduced martensitic phase transformation/detwinning in front of the crack under nominally isothermal loading was observed using synchrotron X-ray diffraction (Stankiewicz et al., 2007; Gollerthan et al., 2009; Daymond et al., 2007), digital image correlation (DIC) (Daly et al., 2007; Haghgouyan et al., 2016), optical microscopy (Creuziger et al., 2008), and IR thermography (Gollerthan et al., 2009). Crack growth in NiTi SMAs under quasi-static mechanical load at nominally constant temperature has been experimentally studied (Stankiewicz et al., 2007; Gollerthan et al., 2009; Vaidyanathan et al., 2000; Robertson and Ritchie, 2007, 2008; Gall et al., 2001) and nearly identical values of critical stress intensity factor K_{IC} \sim 30 MPa $m^{1/2}$ for superelastic NiTi SMAs were calculated based on the applicability of Linear Elastic Fracture Mechanics (LEFM). However, most of the specimens used were not in accordance with ASTM E399 (ASTM E399-17, 2017) for which the small-scale yielding criterion should be satisfied, which in case of SMAs translates into the size of the nonlinear phase transformation/detwinning zone close to the crack tip being smaller than a fraction of the characteristic dimensions of the crack. Recently, efforts have been made towards proposing a methodology for measuring the fracture toughness of SMAs using Jintegral as the fracture criterion by Haghgouyan et al. (2019). This methodology modifies ASTM E1820 (ASTM, 2013) to accommodate the transformation/detwinning-induced changes in the apparent elastic properties of SMAs. Fracture toughness experiments were carried out using near-equiatomic NiTi compact tension (CT) specimens and fracture toughness, J_{IC}, was measured for the first time. It is observed that the fracture toughness of near-equiatomic NiTi is much higher than the value reported based on LEFM. Based on the fracture toughness of SMAs measured in these experiments, crack growth under mode-I isothermal loading was also studied using finite element analysis (FEA) (Haghgouyan et al., 2019, 2018). Good agreement between the experimental and numerical load-displacement responses and fracture toughening behavior, associated with the energy dissipated by phase transformation, was reported during crack extension.

The aforementioned studies dedicated to isothermal mechanical fracture of SMAs nonetheless provide a valuable foundation for understanding fracture under more complex thermomechanical loading paths, typically utilized in solid-state actuator applications. To the best of authors' knowledge, in the only experimental work attempting to understand fracture response of SMAs under actuation loading, *i.e.*, thermal variations under constant external mechanical loading, Iliopoulos *et al.* (Iliopoulos *et al.*, 2017) studied fracture in thin double-notched NiTi specimens. The specimens, initially in austenitic phase, were cooled under constant tensile bias loads maintained at a fraction (as low as 50%) of the isothermal strength of the SMA in pure martensitic state. Unstable crack growth was due to the sudden release of elastic energy stored once a macroscopic crack was initiated. The initiation of crack growth is due to the induced phase transformation during cooling.

Analytical and numerical analysis of crack tip stress fields and crack growth in SMAs subjected to actuation loading has unraveled some of the factors responsible for the unusual thermomechanical fracture response. Crack growth in polycrystalline NiTi SMAs under mechanical and actuation loading has been investigated numerically by the authors (Jape et al., 2018; Baxevanis et al., 2016; Jape et al., 2016a, 2016b; Baxevanis et al., 2014, 2013, 2012; Baxevanis and Lagoudas, 2012) using the phenomenological constitutive models for SMAs (Boyd and Lagoudas, 1996; Lagoudas et al., 2012; Xu et al., 2019, 2021; Karakalas et al., 2019). Baxevanis et al. (2016) studied the near-tip mechanical fields in an infinite medium SMA with a semi-infinite crack subjected to constant far-field tensile load and repeated thermal cycling. The driving force for crack growth was shown to increase substantially during cooling as a result of crack tip anti-shielding due to "global" forward phase transformation in front of the crack, i.e., due to large-scale transformation of a size comparable to the specimen size. The obtained decrease in the driving force during heating was ascribed to crack-tip shielding from reverse phase transformation in front of the crack. Jape et al. (Jape et al., 2016b, 2015, 2014) computationally examined stable crack growth in infinite medium SMA during thermal cycling under constant load, and attributed cracking to the enhancement in driving force for crack growth engendered by global thermomechanically induced phase transformation. Extension of this analysis demonstrated that transformation induced plastic (TRIP) strains due to cyclic thermomechanical loading in SMAs affect the driving force for crack growth and the stable crack growth regime in a similar fashion to that of transformation strains (Jape et al., 2016a, 2018). The effect of TRIP on the overall fracture response of SMAs was shown to be dual in nature: higher TRIP strains not only increase the temperature for initiation of crack growth during cooling but also lead to an apparent fracture toughness enhancement due to irreversible strains behind the moving crack tip.

To summarize, experimental studies on notched NiTi specimens and numerical results from a prototype infinite medium problem have highlighted the key characteristic of fracture of SMAs under actuation loading. The main mechanism behind this response is the increase in driving force for crack growth via stress redistribution due to global forward phase transformation, assisting crack growth during cooling (Iliopoulos et al., 2017; Baxevanis et al., 2016). Stable crack growth was observed in numerical simulations and was attributed to the toughening effect produced by transformed material left in the wake of the moving crack tip that did not reverse transform (Jape et al., 2016a, 2016b). Crack driving force and stable crack growth response was also shown to strongly depend on thermomechanical material parameters and TRIP strain generated during actuation cycles. The existing literature thus provides a fertile ground for further investigation in the area of SMA fracture under actuation loading using systematic experimental and simulation tools.

To this end, in the present work, we experimentally observe stable crack growth in NiTi SMAs under actuation loading for the first time and demonstrate the capability of an existing constitutive model to quantitatively reproduce the experimental results based on the recently measured accurate fracture toughness values. In particular, crack growth characteristics of CT specimens of nearly equiatomic NiTi under actuation loading were first studied experimentally. FEA was then performed on pre-cracked NiTi CT specimens, considering the nonlinear hysteretic thermomechanical constitutive behavior, and stable crack growth was simulated. Numerical results were used to assist the interpretation of experimental data. The experimental data, simulation results, and knowledge base generated in this study is a step forward towards the design and development of reliable solid-state SMA actuators.

The remainder of this paper is organized in the following manner: Section 2 describes the material, specimen geometry and

experimental setup used to conduct the experiments. Then, the experimental results of the crack growth curves obtained from the optical method and strain data from DIC are presented. In Section 3, FEA of the pre-cracked SMA CT boundary value problem is described and simulation results pertaining to crack growth are presented. A discussion and synthesis of the experimental findings and numerical results is then given in Section 4. Finally, the main conclusions drawn from this work are outlined in Section 5.

2. Experiments

2.1. Materials and methods

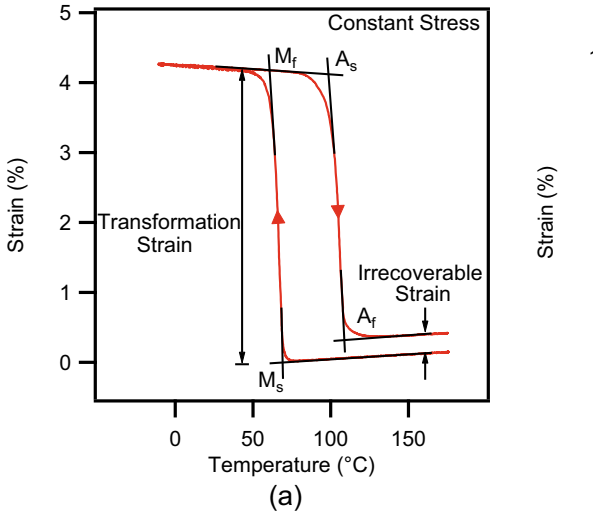
The material used in this study, Ni_{49.5}Ti_{50.5} (at. %) obtained from ATI Metals Inc., was melted using the Vacuum Induction Melting/ Vacuum Arc Melting (VIM/VAR) method, and rotary forged at 800 °C followed by air cooling. For the sake of brevity, the material composition will be reported as Ni₅₀Ti₅₀ in what follows. For thermo-mechanical characterization, thermal cycling experiments under constant tensile stress levels (i.e. isobaric thermal cycling) were carried out using a servo-hydraulic MTS test machine. A dog-bone sample was loaded under uniaxial tension to various load levels and then thermally cycled under constant load (isobaric) conditions. A schematic of strain vs. temperature response and how the transformation characteristics are determined from isobaric tensile experiments is presented in Fig. 1a. Samples were heated and cooled with a rate of 10 °C/min via thermal conduction from the grips. The temperature was measured using a K-type thermocouple directly attached to the gauge section while strain was measured using an MTS high-temperature extensometer. The results are presented in Fig. 1b.

For actuation crack growth experiments, the CT samples, following the ASTM standards as shown in Fig. 2a and b, were used. Because the material was hot rotary forged and all specimens were cut in the same orientation, no significant texture effects are expected (Rodrigues et al., 2017). The samples were heated with a Roy 1500 induction heater and cooled through assisted convection cooling through continuous air flow, all of which were controlled by a Eurotherm 2200 PID temperature controller. The temperature of the sample was measured by averaging the readings from 6 K-type thermocouples spot welded onto the sample

as shown in Fig. 2b. The spread between the thermocouple measurements was at most ± 3 °C and the error for a standard grade K-type thermocouple is ± 2 °C. Crack growth experiments were carried out in MTS-810 test machine. The applied force on the sample and load point displacement were acquired and recorded through the MTS Multi-Purpose Test Suite, and temperatures were recorded in LabView through a Measurement Computing data acquisition board.

To grow sharp cracks, the samples were cycled between P_{min} and P_{max} with a force ratio $R = P_{min}/P_{max} = 0.1$, resulting in an initial stress intensity factor range of $\Delta K = 9 \text{ MPa} \cdot \text{m}^{1/2}$. The pre-cracks were grown until the total crack length (notch length plus fatigue pre-crack) reached ~6 mm. After fatigue pre-cracking, the samples were heated to 170 °C under zero force to fully transform the material into austenite, then loaded to a predetermined force level that was held constant throughout the test. The bias loads resulted in three *initial* J-integral values of J_0 = 11.25, 2.81, and 1.25 KJ/m². These correspond to K_0 values of 30, 15, and 10 MP $_1/m$, respectively. As discussed in a recent work (Haghgouyan et al., 2019), to account for the martensitic transformation/martensite orientation-induced changes in the apparent elastic properties of SMAs, the J-integral can be calculated as the sum of elastic and inelastic components as $I = I^{el} + I^{in}$, where $I^{el} = \eta^{el} A^{el} / Bb$, and $I^{in} = -I^{el} A^{el} / Bb$ ηⁱⁿAⁱⁿ/Bb. This differs from the standard method developed for conventional elastic-plastic materials where the elastic component of J is calculated using stress intensity factor and Young's modulus. Here B is the specimen thickness, b is the length of the unbroken ligament (b = W-a, where W and a are the specimen width and crack size, respectively); Ael and Ain are the elastic and inelastic components of the area under the load-displacement curve, respectively; η^{el} and η^{in} are geometry-dependent factors (Haghgouyan et al., 2019). For the applied bias load levels, $J_{in} = 0$ since the stress-induced transformation is restricted to a small region close to the crack tip, i.e., small-scale transformation conditions and in turn LEFM prevail. Thus, the initial J-values are equal to G-values (energy release rate) and can be translated to K-values (stress-intensity factor) by employing well-known formulas.

The temperature was cycled with 10 min of heating to the Upper Cycle Temperature (UCT) of 170 °C, followed by a 2-minute hold, then 10 min of cooling to the Lower Cycle Temperature (LCT) of 35 °C, followed by an 8-minute hold. UCT was chosen to ensure complete transformation because transformation



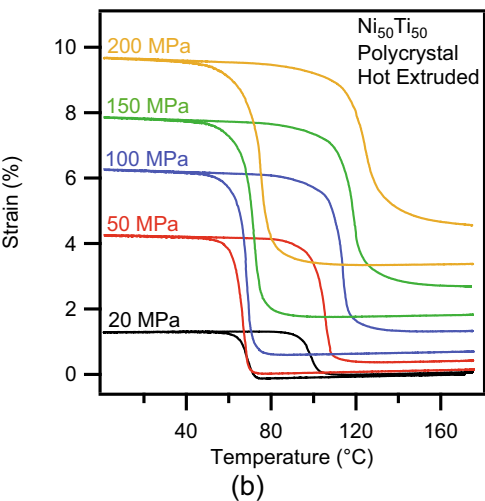


Fig. 1. (a) Schematic representation of strain vs. temperature response of a NiTi SMA under a constant tensile stress, and how the transformation characteristics are determined from thermal cycling experiments under constant stress levels; (b) Strain vs. temperature response of Ni₅₀Ti₅₀ (at.%), hot extruded, polycrystalline dog bone shaped samples during thermal cycling under different tensile stress levels.

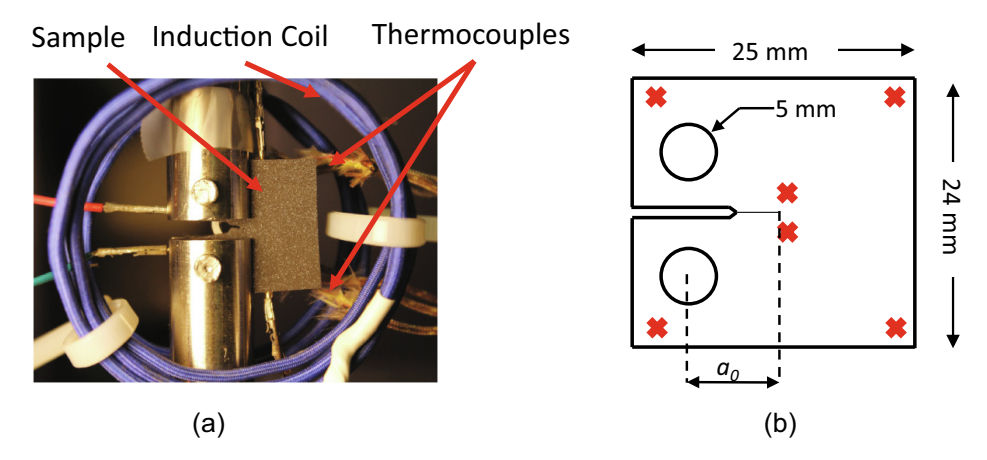


Fig. 2. (a) The experimental setup utilized in this study showing the compact tension (CT) specimen with induction coils around it. Thermocouples were spot welded to the backside of the specimen and can be seen on the right. The speckle-pattern was applied on the specimen surface in order to measure strains using Digital Image Correlation (DIC); (b) schematic of thermocouple positions and the in-plane dimensions of the CT samples with a thickness B of 3 mm and pin hole diameters of 5 mm. A pre-crack starting from the end of the machined crack length is shown (5.5 mm < a_0 < 7.5 mm). Thermocouple locations are marked with red Xs. (For interpretation of the references to colour in this figure legend, the reader is referred to the web version of this article.)

temperatures increase with applied stress, according to the Clausius-Clapeyron relationship. Images from the crack face were recorded during the experiments with a DSLR camera with an optical resolution of 0.02 mm/pixel. Crack length was determined by taking the straight-line distance between the end of the machined notch and the end of the visible crack tip and adding that to the distance between the end of the machined notch and the load line. It should be noted that the crack length appeared to decrease upon heating which was due to the closure of the crack. The uncertainty in open crack length measurements is expected to be less than 10 times the optical resolution, *i.e.*, less than ±0.2 mm. A schematic of the sample and the crack tip at certain temperatures is shown in Fig. 3. Note that during cooling, the transformation zone region close to the crack tip expands and LEFM eventually do not hold.

2.2. Experimental results

2.2.1. Stable crack growth

In this section, the experimental results from the crack growth measurements in the CT specimens under constant mechanical loading and varying temperatures are presented. Three J_0 values were considered on six samples as shown in Table 1. First, a constant tensile load corresponding to J_0 of $11.25~{\rm KJ/m^2}$ was applied while the material was in the austenitic phase, followed by thermal cycling between UCT and LCT. With this initial loading condition, crack growth was triggered when the temperature of the sample reached $\sim\!77~{\rm ^{\circ}C}$ during cooling.

Stable crack growth was observed during first cooling cycle in all cases where, once crack growth was triggered, further cooling was required to extend the crack. Steady-state crack growth was

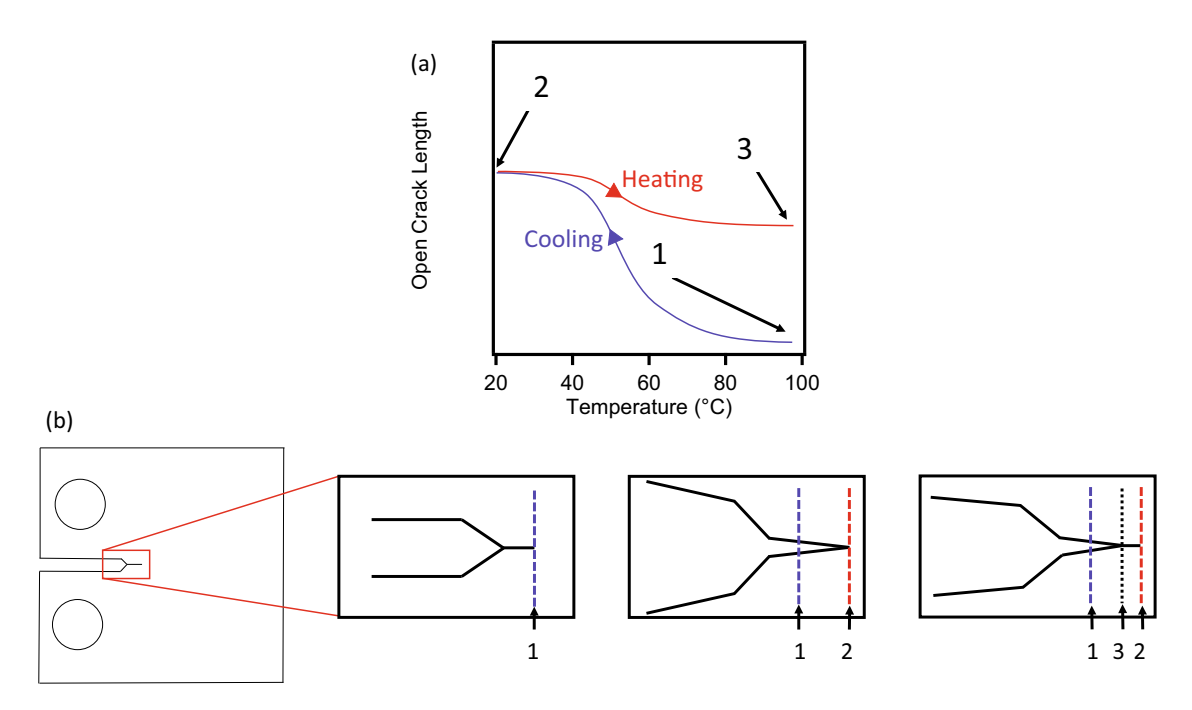


Fig. 3. The schematics showing the crack opening and closing as a function of temperature across reversible martensitic transformation during a thermal cycle and corresponding crack growth stages; (a) a representative heating–cooling cycle, and the crack extension during thermal cycling; (b) crack growth from point 1 to point 2 during cooling; upon heating, the crack faces close and the measurable crack length shortens to point 3.

Table 1 List of all tested $Ni_{50}Ti_{50}$ hot extruded, polycrystalline compact tension samples. Three different bias load levels corresponding to J_0 are listed, as well as the number of complete temperature cycles (Upper Cycle Temperature to Lower Cycle Temperature and back) and the average crack growth rate in mm/cycle.

Sample	J ₀ (KJ/m ²)	Cycles to Failure	Crack Growth Rate (mm/cycle)
1	11.25	<1	N/A
2	11.25	<1	N/A
3	2.81	6	0.86
4	2.81	5	1.14
5	1.25	17	0.34
6	1.25	16	0.39

also observed followed by ultimate failure of the samples due to unstable crack growth. Experimentally measured crack lengths as a function of temperature for all three different J_0 cases can be seen in Fig. 4a, b, c, left column, while accompanying Fig. 4d, e, f, right column, show the results from the corresponding numerical simulations using finite element analysis (FEA). Simulation results closely match the experimental data and are introduced and explained in greater detail in Section 4.

For lower constant bias loads and associated J₀ levels, stable crack growth was observed under multiple thermal cycles before ultimate failure occurred. Samples 3 and 4 were tested under a constant load corresponding to $J_0 = 2.81 \text{ KJ/m}^2$ and crack extension as a function of temperature for Sample 4 can be seen in Fig. 4b. Once the sample reached a specific critical temperature during cooling (~70 °C in this loading case), crack growth was triggered and crack extended by ~0.2 mm in a stable manner until another critical temperature was reached, where crack arrest occurred at uniform temperature of about 60 °C. The sample was then cooled to the LCT without any further crack extension. When the sample was subsequently heated up to the UCT, partial crack closure instead of crack growth was observed during heating. At UCT, the sample was again cooled for a second thermal cycle and crack growth was triggered during cooling. Subsequent stable crack growth of 0.2 mm by the end of the second cooling cycle was followed by crack closure during heating. As the sample was subjected to subsequent thermal cycles, stable crack growth was always observed during cooling. Moreover, crack growth was triggered at a higher temperature during each cycle, owing to the progressive increase in initial crack length at the beginning of every thermal cycle. The sample sustained stable crack growth through 6 complete thermal cycles followed by ultimate failure due to unstable crack growth and a final reported crack extension of approximately 5.5 mm (Fig. 4b). Accompanying plot in Fig. 4e shows the results from the simulation, where overall fracture behavior was similar to that observed in experiments, but crack growth progressed through 8 thermal cycles before reaching ultimate failure with a final crack extension of \sim 6.5 mm.

Finally, samples 5 and 6 were tested at the lowest bias load with $J_0 = 1.25 \text{ KJ/m}^2$. Crack extension for sample 5 as a function of temperature is plotted in Fig. 4c. In this loading condition, crack started to grow during the first cooling cycle at a critical temperature of \sim 62.5 °C. Stable crack growth was again observed as the temperature decreased from approximately 62.5 °C to 55 °C, increasing the crack size by approximately 1.25 mm. Similar to the previous loading condition, crack arrest occurred once temperature reached 55 °C and cooling continued till LCT; heating from LCT to UCT resulted in partial crack closure without any further crack extension. During subsequent thermal cycles, repeated crack growth was observed: stable crack extension followed by crack arrest during cooling and partial crack closure during heating. Crack extended through 18 complete thermal cycles, and during the 19th cooling cycle, became unstable resulting in ultimate failure. Fig. 4f shows crack extension as a function of temperature from the numerical simulations where the fracture response shows similar features: crack growth was triggered and extended by a limited amount during cooling, critical temperature for crack extension increased with each cycle, and crack growth occurred through 19 complete thermal cycles before the specimen reached final failure in the 20th thermal cycle. Further details of the finite element simulations are provided in Section 4.

2.2.2. Local strain fields using DIC

Digital Image Correlation (DIC) technique was used to measure the 2D strain field during the experiments. The experimentally measured contours of in-plane normal and shear strains are shown in Fig. 5. For the sake of brevity, the cycle just before the failure in J_0 = 1.25 KJ/m² case is considered. The results at four temperatures (100, 85, 70, and 35 °C) are presented from DIC and FEA simulations. At 100 °C, before extensive martensitic transformation has begun in the entire sample, the high tensile ε_{yy} strain in the loading direction at the crack tip is attributed to stress-induced martensitic transformation due to the applied mechanical load and residual strain from previous cycles. On the opposite end, where the specimen experiences compression, a small region of compressive strain is generated. The ε_{xx} component in the crack growth direction, on the other hand, shows a relatively small value at 100 °C.

As the sample cooled down to 85 °C, the crack extended, and a significant amount of tensile ε_{vv} strain is generated near the crack tip. Additionally, as the temperature is lowered, the crack mouth opening increases as compared to that at high temperature. Tensile ε_{xx} region at 85 °C shows modest increase as the crack tip experiences increased loading due to forward phase transformation. On the other hand, the absolute magnitude of the ε_{xy} shear component observed from DIC shows modest increase in the crack tip region (<1% strain). With further decrease in temperature in the specimen (70 °C), the region of near-tip tensile ε_{yy} strain increases in size due to more material undergoing thermally induced forward phase transformation, and the crack extends further. Moreover, the high ε_{vv} strain region also extends towards the pinholes due to high contact stresses between the sample and the pins. The ε_{xx} tensile strain at this point shows a significant increase in magnitude in a region roughly parallel to the crack path, extending to the back of the specimen. Compressive ε_{xx} strains are generated at the top and bottom faces of the specimen due to compressive loading experienced by those regions. At 70 °C, the DIC images continue showing a modest increase in the magnitude of the shear ε_{xy} strain around the crack tip region ($\pm 2\%$) in a classical "butterfly" shape where the region above the crack tip shows positive values (up to +3%) whereas the region below the crack tip shows negative values (up to -3%). Subsequent decrease in temperature (35 °C) leads to a significant increase in the size of high tensile ε_{vv} strain zone in the near crack tip region driven by large scale phase transformation, that results in further crack extension, and is associated with stable crack growth until the LCT was reached. Similar increase is observed in the region of high tensile ε_{xx} strain field both in front of the crack tip and in the regions adjoining the crack faces. Moreover, the compressive ε_{xx} region observed on the top and bottom specimen faces at 70 °C extended considerably as the temperature reached 35 °C. At this temperature, the region of prominent shear strain ε_{xy} (absolute magnitude > 4%) in DIC contours expands in size when temperature decreases to 35 °C, maintaining a similar distribution from higher temperatures. At this temperature even with large tensile strains (ε_{xx} and ε_{yy}) present at the crack tip, crack growth is arrested because any further generation of transformation strain in the sample ceases and the driving force for crack growth remains constant. Note that the crack growth arrest occurs before reaching LCT at a slightly higher temperature (~40 °C), as shown in Fig. 4c.

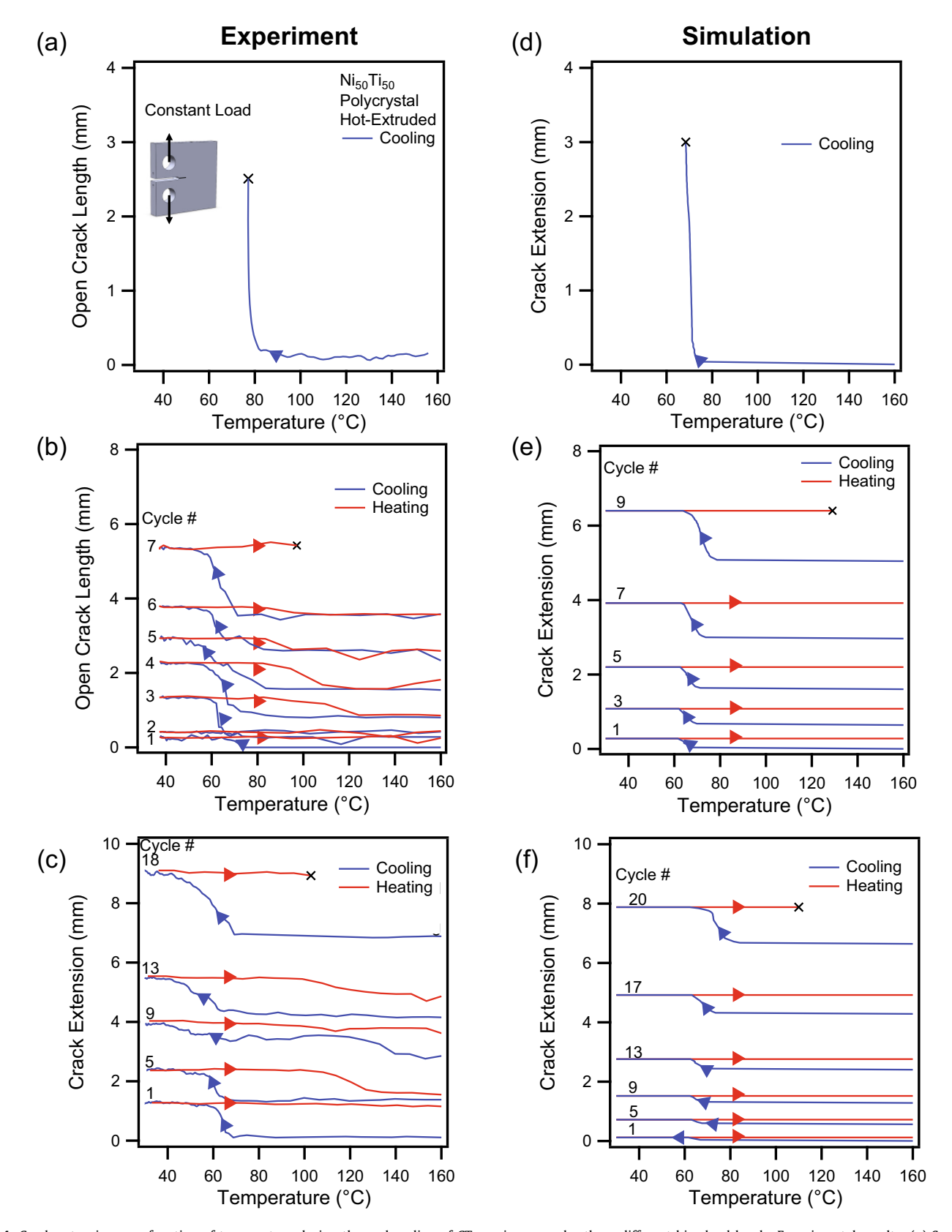


Fig. 4. Crack extension as a function of temperature during thermal cycling of CT specimens under three different bias load levels. Experimental results: (a) Sample 1, $J_0 = 11.25 \text{ KJ/m}^2$, failed in the 1st cycle during cooling; (b) Sample 4, $J_0 = 2.81 \text{ KJ/m}^2$, failed in the 7th cycle during heating; (c) Sample 5, $J_0 = 1.25 \text{ KJ/m}^2$, failed in the 18th cycle during heating. Numerical results: (d) $J_0 = 11.25 \text{ KJ/m}^2$, failed in the 1st cycle during heating; (e) $J_0 = 2.81 \text{ KJ/m}^2$, failed in the 9th cycle during heating; (f) $J_0 = 1.25 \text{ KJ/m}^2$, failed in the 20th cycle during heating.

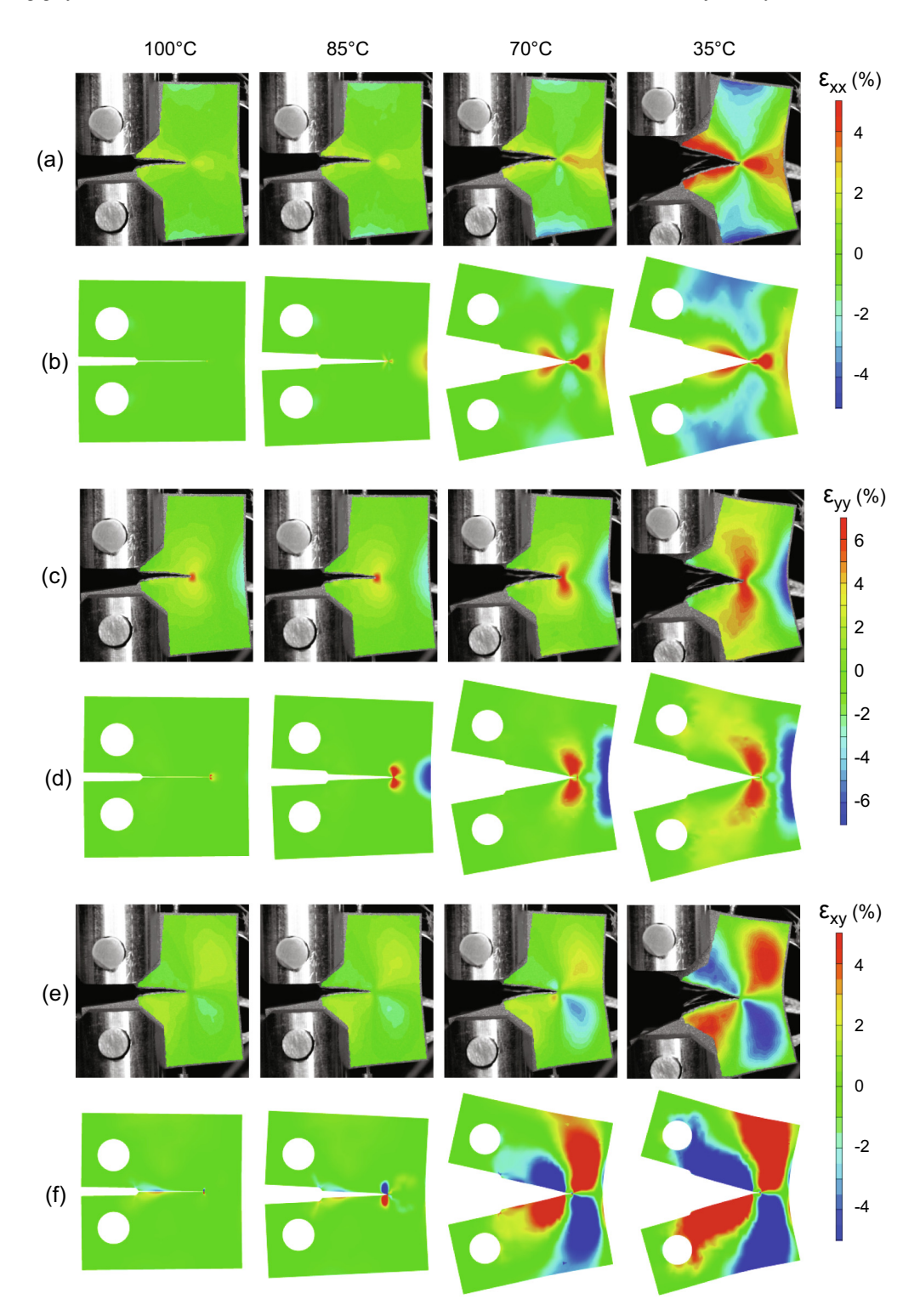


Fig. 5. In-plane strains (ε_{xx} , ε_{yy} , ε_{xy}) during the last thermal cycle before failure for J_0 = 1.25 KJ/m² case at 100 °C, 85 °C, 70 °C, and 35 °C obtained using DIC (a, c, e) and FEA simulations (b, d, f).

2.2.3. Fracture surface evolution

Micrographs were obtained using scanning electron microscopy (SEM) to identify features on the fracture surface (Fig. 6). For the sake of brevity, the images from one sample (Sample 3) are presented. Note that the overall fracture surface shows quasicleavage features. There is also a difference in the types of fracture surfaces of the fatigue pre-cracking and those of the actuation crack

growth. The fatigue pre-cracked region appears to have striations coming in from the outside corners of the specimen and are much smoother than the sections fractured by actuation. In contrast, the actuation crack fracture surfaces seem much rougher and do not have as clear of a defined crack growth direction, other than from left to right. Higher magnification images show relatively flat fracture surfaces, which is again indicative of quasi-cleavage fracture.

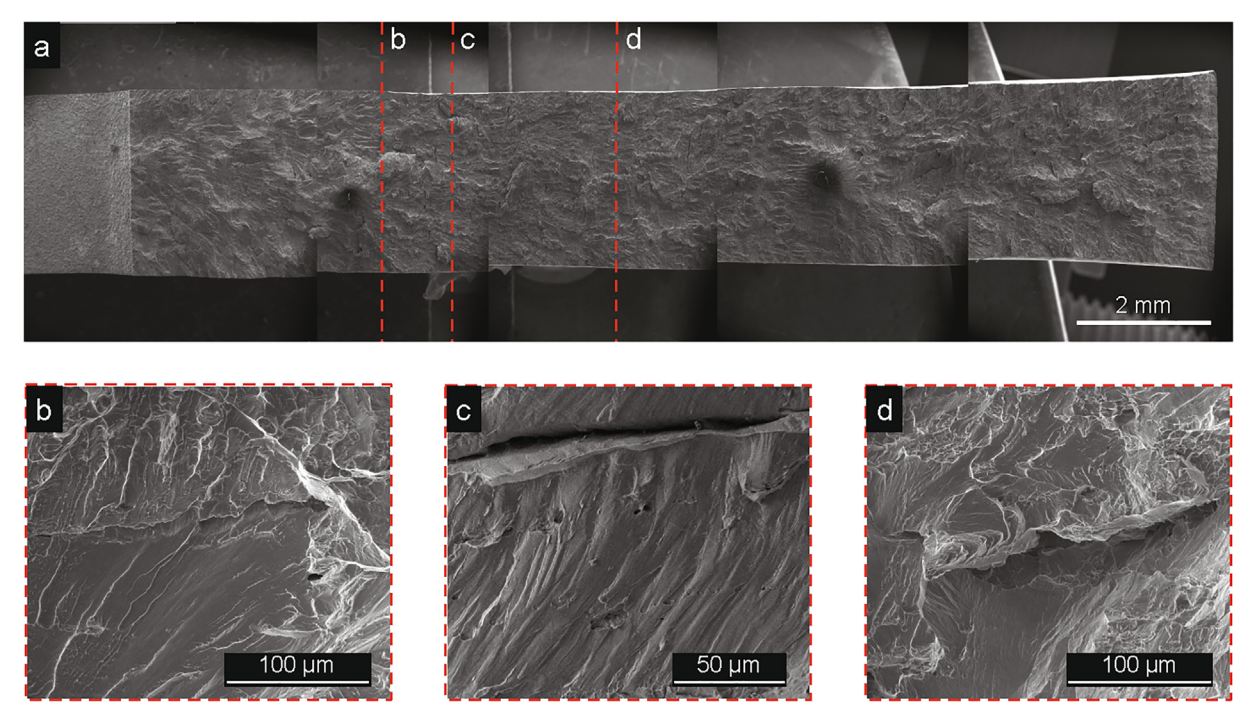


Fig. 6. Scanning electron microscopy (SEM) images of the fracture surface of Sample 3: (a) assembly of low magnification images to assess whole fracture surface; location of higher magnification images and the end of the crack growth at each cycle are also marked; (b)- (d) higher magnification images taken at the points of the end of crack growth

3. Finite element analysis

3.1. Formulation of the boundary value problem

The two-dimensional (2D) numerical boundary value problem of a polycrystalline NiTi CT specimen with a pre-existing crack subjected to thermal actuation loading, mimicking the experimental setup in Section 2.1, has been formulated. Based on previous work (Baxevanis et al., 2016; Jape et al., 2016a, 2016b), we used an energetics based fracture criterion with the crack tip energy release rate as a single parameter for fracture toughness. Abaqus FEA suite was used to solve the numerical boundary value problem and to simulate crack growth under constant mechanical load and thermal actuation. The results obtained were compared with the experimental data.

A schematic of the numerical boundary value problem formulated to simulate the crack growth experiments is shown in Fig. 7, where the geometry and overall dimensions of the CT specimen are adopted from the fracture experiments. Thermoelastic and phase transformation material properties of the NiTi SMA are calibrated from uniaxial tensile tests on dog bone specimens of the NiTi material used for the fracture experiments (Fig. 1). Thermomechanical constitutive behavior of the NiTi SMA is described by the phenomenological model developed for polycrystalline SMAs undergoing diffusionless solid-state phase transformations based on a continuum thermodynamics framework (Boyd and Lagoudas, 1996; Lagoudas et al., 2012). This material model is implemented in the Abaqus implicit finite element solver using a user-defined material subroutine (Abagus Analysis User's Manual, 2017). Details of this model are presented in an appendix to the paper and the material parameters used to calibrate the model are presented in Table 2. The computational domain is symmetric across the fatigue pre-crack and the two crack faces are bonded in the region representing the unbroken ligament where crack propagation is expected to occur, and separated in the region

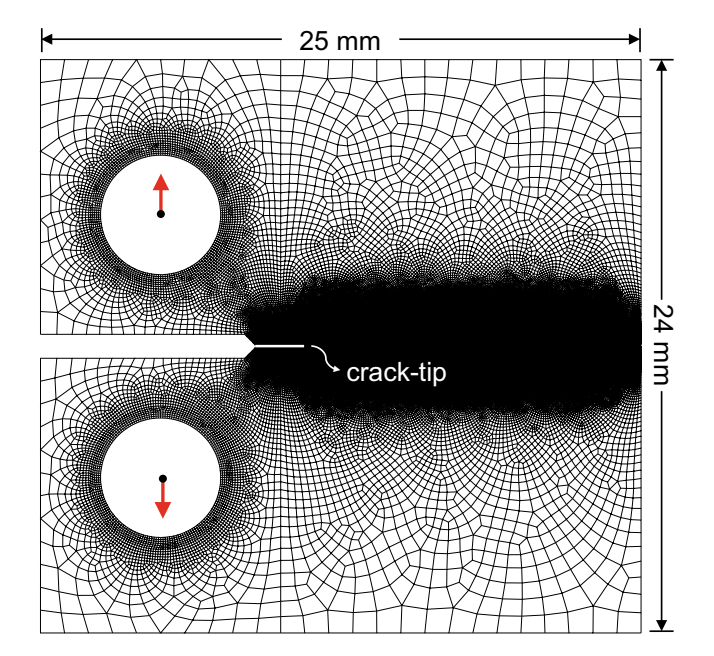


Fig. 7. Boundary value problem representing the NiTi CT specimen under experimental investigation with location of the pre-crack and the predetermined direction of crack propagation under mode-I loading.

where the specimen is pre-cracked (Fig. 7). Virtual crack closure technique (VCCT), based on Irwin's crack closure integral (Krueger, 2004; Rybicki and Kanninen, 1977; Irwin et al., 1958), is utilized to model mode-I crack propagation under combined thermo-mechanical loading. Crack tip energy release rate is used as the driving force for crack growth and is calculated from nodal forces and displacements using VCCT (Krueger, 2004). Note that while the simulations are performed under actuation loading path,

 Table 2

 Material parameters used in finite element simulations.

Parameter	Value	Parameter	Value
1 di dillictei	value	i didilictei	value
E _A	80 GPa	M_s	67 °C
E_{M}	62 GPa	$M_{\rm f}$	58 °C
v_A	0.33	A_s	94 °C
v_{M}	0.33	A_f	106 °C
H_{sat}	6%	C_A	8 MPa/°C
k	$0.026~{\rm MPa^{-1}}$	C_{M}	15 MPa/°C

the material-specific critical fracture parameter was obtained from isothermal fracture toughness experiments (Haghgouyan et al., 2019). This assumption can be justified by recognizing that the microstructure close to the crack tip, that of "oriented" martensite, either due to detwinning or stress-induced martensite transformation, is very similar in both cases. Considering elastically deforming martensite at the crack tip, the critical energy release rate is assumed to be equal to fracture toughness of martensite J_{lc} = 136 KJ/m². Given that the crack grows in an "opening mode" under tensile load in a CT specimen, the crack path is assumed to be parallel to the crack plane and orthogonal to the specimen thickness. To accurately capture the crack tip mechanical fields, a highly refined mesh is generated near the predetermined crack path with 2D linear, quadrilateral, plane stress finite elements with reduced integration (CPS4R in Abaqus) and stiffness-based hourglass stiffness. It is also worthwhile to point out that nonlinear geometric effects due to large rotations of the CT specimen are accounted for in the finite element model using the NLGEOM option in Abagus that utilizes a large displacement/ large rotation formulation (Abagus Analysis User's Manual, 2017). During thermomechanical loading, as the energy release rate at the crack tip node increases during loading and reaches the material-specific critical value, node debonding occurs and the crack extends incrementally by the length of one crack tip element in the predetermined direction. Further increase in the crack driving force results in subsequent separation of crack tip nodes and incremental propagation of the crack until there is no further increase in the driving force.

A quasi-static analysis of thermomechanical loading of the SMA CT sample is conducted. First, to ensure that the material is in pure austenitic phase, a uniform temperature field of 170 °C is prescribed at every material point in the CT specimen. To simulate mode-I tensile loading condition, a constant load is applied at one pin location and the other pin location is assumed to undergo no displacement along any direction but is allowed to freely rotate (Fig. 7). Pin locations represent the center of the loading pins in the experimental setup and the top and bottom hole surfaces are kinematically constrained to follow the movement of these pins. Due to the applied bias load, faces of the pre-crack open and the crack tip experiences an elevated stress state, resulting in a small region of stress-induced martensitic transformation (SIM). Following the application of a constant bias load, the entire SMA specimen is subjected to a temperature change from UCT (170 °C) to LCT (35 °C) at a thermal rate low enough to maintain a uniform temperature field in the material. Cooling of the specimen to LCT is then followed by uniform heating back to UCT. Repeated thermal cycling between UCT and LCT is carried out until specimen undergoes catastrophic failure, and crack growth during each cycle is calculated. This analysis is performed for three different bias load levels corresponding to the J₀ described in the experimental section and the results are presented in Section 4.

3.2. FE results

In the finite element simulation of crack growth, when the CT specimen is uniformly cooled, forward phase transition gives rise

to transformation strains in front of the crack tip which tend to amplify crack opening and increase the driving force for crack growth (Fig. 8). The increase in the crack tip opening displacement during cooling and under constant force has already been reported for NiTi in numerical simulations (Baxevanis et al., 2016) and experiments (LePage, 2018). Large-scale phase transformation thus increases the driving force and when it reaches a material specific critical value, crack growth occurs (Jape et al., 2016a, 2016b). Moreover, since crack growth occurs in regions of stress induced martensite, fracture toughness of pure martensite, which has been experimentally evaluated to be ~136 KJ/m² (Haghgouyan et al., 2019); is utilized as the material specific critical value for crack growth under actuation loading conditions. It is important to note that crack growth is triggered during cooling in every loading case and proceeds through single or multiple thermal cycles, depending on the initial bias load.

3.2.1. Stable crack growth

Crack extension is plotted with respect to the uniform temperature in the NiTi CT specimen during cooling in Fig. 4d-f. At $J_0 = 11.25 \text{ KJ/m}^2 \text{ (Fig. 4d)}$, crack growth is triggered when the temperature in the specimen reaches ~74 °C during cooling, and subsequent cooling is required to further extend the crack. Stable crack growth behavior can be attributed to toughness enhancement resulting from transformation strains left in the wake of the crack (Jape et al., 2016a, 2016b). Overall crack extension in the stable crack growth regime is approximately 3 mm. Following stable crack growth steady state is attained when uniform temperature in the specimen reaches ${\sim}69\,^{\circ}\text{C}$ and ultimate failure of the specimen due to unstable crack growth occurs. When the external bias load is $J_0 = 2.81 \text{ KJ/m}^2$, the crack extension is triggered in the first cooling cycle when temperature in the specimen reaches approximately 69 °C (Fig. 4e). Stable crack growth is observed as the specimen is further cooled and crack arrest occurs at 63 °C after the crack tip has moved by a small distance (about 0.25 mm). Crack arrest can be attributed to the saturation in driving force for crack growth due to completion of forward phase transformation in front of the crack tip, and subsequent initiation of phase transformation behind the crack tip. Further cooling to LCT occurs without any

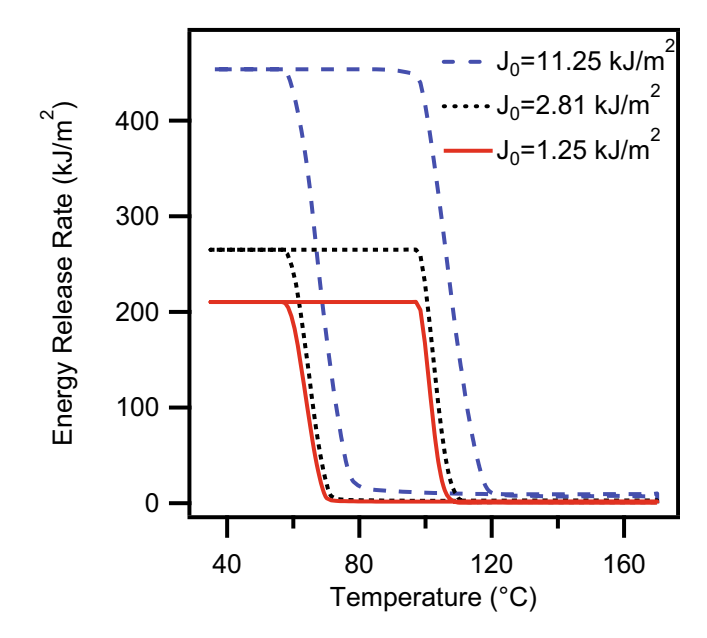


Fig. 8. Evolution of the crack tip energy release rate for a stationary crack obtained from FEA simulations during complete thermo-mechanical cycling between the lower cycle and upper cycle temperatures for J_0 = 11.25, 2.81, 1.25 KJ/m².

change in state of the crack tip. As the entire specimen is then heated to UCT, large scale reverse transformation into austenite occurs, and no crack growth is observed during heating. During the second cooling cycle, crack grows by approximately 1 mm and crack growth cessation similar to that in the first thermal cycle is observed. Specimen is again heated from LCT to UCT leading to recovery of the transformation strains without any further crack extension. Throughout the simulation, crack propagates through 8 complete thermal cycles, always during cooling, until final failure due to unstable crack growth occurs in the 9th heating cycle. Throughout the stable crack growth regime, crack extends by approximately 6 mm. Two main features of the crack growth response are noted: (i) the event of triggering of crack growth occurs at a higher critical temperature, primarily due to an enlarged initial crack at the beginning of each subsequent cycle (Fig. 9), and (ii) the amount of crack extension in the stable growth regime increases with each cycle.

Finally, the external bias load is further reduced to the lowest level used in this study such that J_0 = 1.25 KJ/m². At the lowest J_0 , as shown in Fig. 4f, crack growth is first triggered at $\sim\!63\,^{\circ}\text{C}$ and the crack tip moves by <1 mm during the first cooling cycle. In the subsequent thermal cycles, crack propagates through 19 complete cycles to a final length of approximately 8 mm, until failure occurs in the 20th heating cycle. The characteristics of crack growth response in this loading case are qualitatively similar to that of J_0 = 2.81 KJ/m², including the trends in critical temperature for triggering of crack extension and the amount of stable crack growth in each cycle.

3.2.2. Strain field and martensite volume fraction

Contour plots of the in-plane normal and shear strains for the case of constant bias load for $J_0 = 1.25 \text{ KJ/m}^2$ are shown in Fig. 5. Crack opening, as a result of the anti-shielding effect due to phase transformation strains in front of the crack tip, is seen at low temperature. Significant tensile ε_{yy} strain (6–8%) is generated in the near crack tip area in the classical plane stress shape where the initially austenitic material undergoes stress induced martensitic

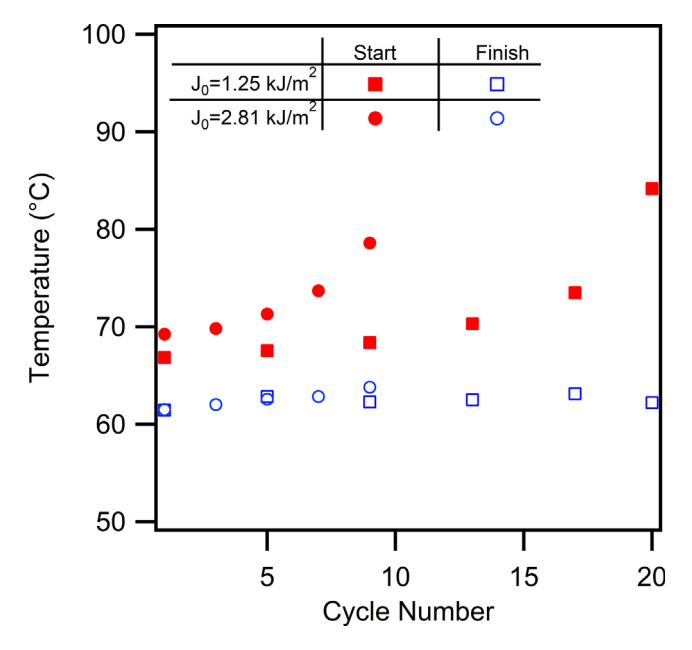


Fig. 9. Evolution of the crack growth start and finish temperatures for all three cases. The critical crack growth start temperatures tend to increase with each cycle, primarily due to an enlarged initial crack at the beginning of each subsequent cycle. The critical crack growth finish temperature does not have as pronounce of an increase in either the $J_0 = 1.25$ or 2.81 kJ/m^2 cases.

transformation. On the opposite side of the specimen, compressive strains are generated due to the phase transformation occurring under a compressive stress state. These results match with those obtained from the experimental data from DIC for all loading cases, including for $J_0 = 11.25 \text{ KJ/m}^2$ and 2.81 KJ/m² which are not shown for the sake of succinctness. The $\varepsilon_{\rm xx}$ strain component shows no significant value earlier in the cycle at 100 °C but increases to \sim 2% when the temperature falls to 85 °C. Further cooling of the sample to 70 °C and then to 35 °C shows an increase in the absolute magnitude (\sim 4%) and extent of the ε_{xx} strain field. At lower temperatures, due to tensile loading on the crack faces, ε_{xx} shows a high magnitude (4%) on the crack faces, in the region close to the crack tip, and at the opposite side of the specimen. Moreover, prominent compressive ε_{xx} strain (-4%) is observed on the top and bottom faces of the specimen due to compressive loading in that region. These FEA results also follow the trends observed in DIC measurements discussed earlier. At 100 °C. FEA contours show a small concentrated region of ε_{xy} shear component with high absolute magnitude (>4%) near the crack tip. As the temperature reduces to 85 °C, this region of high magnitude shear strain expands gradually behind the crack tip, with positive values (>4%) developing below the crack plane and negative values (<-4%) developing above the crack plane. At 70 °C, this distribution of shear strains behind the crack tip further expands in size. Additionally, at this point, a positive shear strain above the crack plane and a negative shear strain below the crack plane develop in front of the crack tip, mimicking the experimental observations. Further decreasing the temperature to 35 °C results in significant expansion of the high shear strain in front and behind the crack tip as seen in the figure. It should be noted that FEA results at all temperatures show significantly higher shear strain magnitudes when compared with DIC results.

The distribution of the martensite volume fraction (ξ) is plotted at the corresponding points of high (100 °C, beginning of crack growth), intermediate (85 °C, 70 °C stable crack growth) and low (35 °C, steady state crack growth) temperatures, in Fig. 10. Martensite volume fraction goes from 0 (pure austenite, blue) to 1(pure martensite, red) when SMA undergoes forward phase transformation, and vice versa during reverse phase transformation. Transformation zone due to SIM is initially limited to a small region near the crack tip; its size varies in each case and is proportional to the initial bias load (Fig. 10a, b, c at 100 °C). During further cooling, regions in front of the crack tip transform from austenite to martensite (Fig. 10a, b, c at 85 °C). Depending on the extent of the growing transformation zone during cooling, crack driving force is elevated and drives further crack extension. As the crack grows with decreasing temperature in the specimen, transformed material is left in the wake of the crack and provides the apparent toughening effect manifested in the form of stable crack growth (Fig. 10a, b, c at 70 °C). Finally, when all of the material has transformed into martensite, crack arrest occurs, and no crack growth is observed until the beginning of the next cooling cycle (Fig. 10a, b, c at 35 °C). Compressive stress at the opposite end of the specimen also result in martensitic transformation and is shown in terms of high values of ξ . It is thus obvious that the initial bias load has a strong influence on the crack growth response and the total number of thermal cycles required to reach steady state crack growth. Lower initial bias load results in relatively smaller zones of fully transformed material in front of the crack tip, resulting in nominally "sub-critical" crack growth. In each thermal cycle, as cooling of the specimen drives forward phase transformation, the crack only grows in small increments due to insufficient increase in the driving force, and crack propagates through multiple thermal cycles. The contours of martensite volume fraction denoting the zones of phase transformation show a characteristic behavior during crack propagation and are qualitatively similar in all loading cases examined.

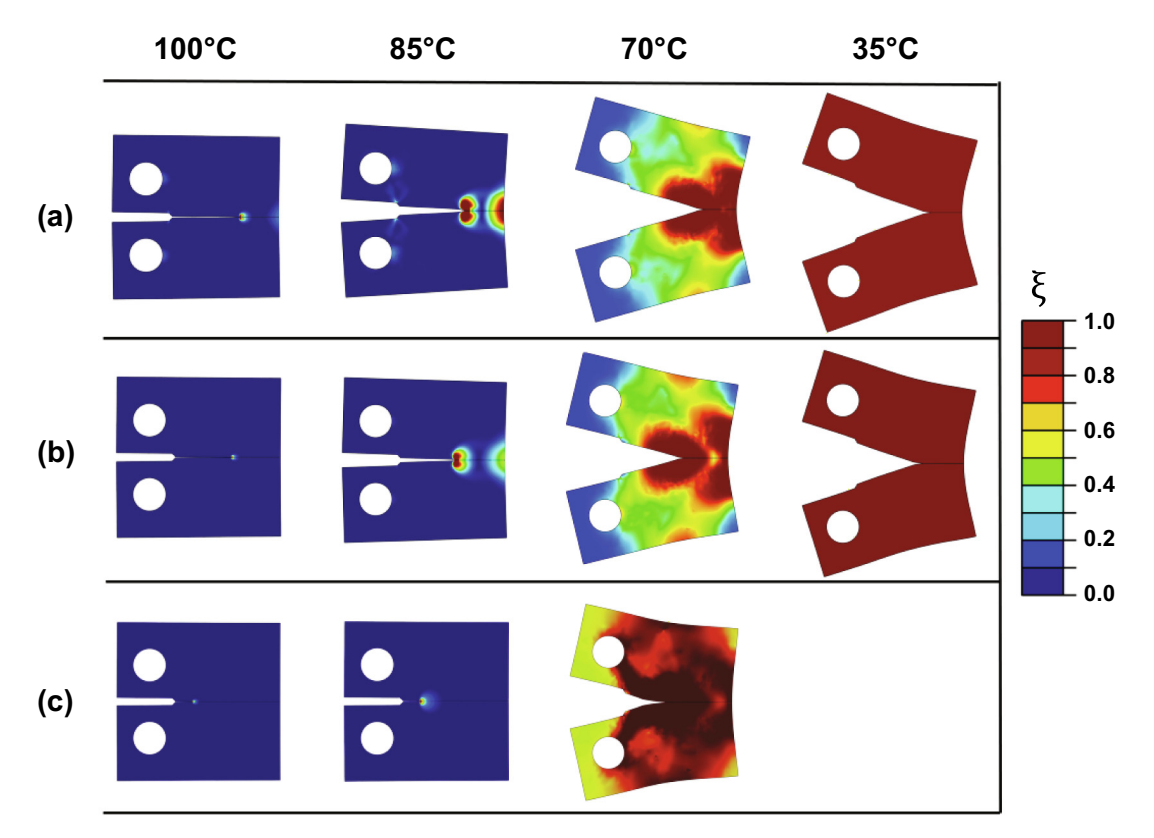


Fig. 10. The contour maps of the martensite volume fraction ξ (ξ = 0 represents pure martensite phase, ξ = 1 represents pure austenite phase, and 0 < ξ < 1 represents the mixed phase) obtained from FEA simulations during the last cooling cycle at various temperatures in the NiTi CT specimens for: (a) J_0 = 1.25 kJ/m², (b) J_0 = 2.81 kJ/m², and (c) J_0 = 1.25 kJ/m².

4. Experimental data vs simulations and discussion

According to the experimental data and numerical results presented in the preceding sections, nearly-equiatomic NiTi specimens undergo crack extension and failure during thermal cycling within a temperature interval sufficient for reversible phase transformation under a constant tensile load. Interestingly, this load level is only a fraction of the corresponding isothermal load needed for fracture at the higher temperature of this interval, with crack advance taking place from the very first cooling. Thus, the observed response may be viewed as an interrupted overload fracture rather than fatigue and as such there is no need for an empirical relation, such as Paris equation, to simulate crack growth. As outlined in our previous works (Iliopoulos et al., 2017; Jape et al., 2018, 2016a, 2016b; Baxevanis et al., 2016), this material response is unexpected as thermal contraction during cooling, coupled with the observed fracture toughness enhancement associated with phase transformation under isothermal loading (Young et al., 2019), is expected to provide crack shielding as opposed to promoting crack extension. Crack growth is always triggered during cooling under every bias load and the crack remains static upon further cooling once phase transformation is completed. Furthermore, the crack grows in every cycle following the initiation of crack advance. As already discussed in Haghgouyan et al. (2019), the mismatch between austenite and martensite elastic stiffness and the associated difference between their measured fracture toughness of approximately 15% should be ruled out as the major factors contributing to the observed response. Moreover, the temperature dependence of the plastic deformation properties—the difference between the yield strength of martensite and austenite is about 20-30%- is not sufficient to explain the low bias load levels needed for crack advance in comparison to the isothermal load level needed for crack growth at the beginning of cooling.

The correlation between the experimental data and numerical results obtained from FEA, when the overall fracture response of the NiTi CT specimens is considered, provides confidence in the insight gained from the constitutive response alone in our previous numerical investigations (Jape et al., 2018, 2016a, 2016b; Baxevanis et al., 2016). Based on those studies, cooling under dead-load condition leads to large scale phase transformation in front of the crack which is the main reason for the substantial increase in the driving force for crack growth. It is only during forward phase transformation that the driving force can reach a critical level and promote crack growth. Interestingly, this phenomenon of rising crack driving force during cooling occurs as transformation strains in front of a stationary or growing crack experience an increase due to thermal or mechanical loading. However, what distinguishes a growing crack tip from a stationary crack is the toughening effect the growing crack experiences due to transformation strains behind the crack tip, resulting in stable crack growth. The observed stable crack growth can thus be attributed to the shielding effect of the transformed material left in the wake of the growing crack, which results in a situation where further cooling is required for crack extension. The shielding effect of the transformed material in the wake of the crack is lost when the material is heated back to austenite and, thus, subsequent cooling results in further crack growth due to the larger crack length as compared with the previous cycle, which explains why the crack grows in every cycle following the initiation of crack advance. It should be noted that as the transformation strains are recovered during heating, both in front and behind the crack tip, the corresponding shielding and anti-shielding effects, respectively, are both progressively lost. However, the shielding is completely lost within a smaller temperature range than that required for the complete loss of anti-shielding; smaller load levels in general behind the crack tip. Thus, even if crack growth is triggered during heating,

as observed numerically in past analyses (Baxevanis et al., 2016; Jape et al., 2016a, 2016b), it is very limited.

The bias load, as expected, has a significant effect on the crack growth response of SMAs. The lower the bias load, higher the number of cycles the CT specimen undergoes before final failure and thus lower the rate of crack growth. Numerical simulations show that the number of cycles to final failure (9 and 20 full thermal cycles to failure for $J_0 = 2.81 \text{ KJ/m}^2$ and 1.25 KJ/m^2 , respectively) are close to that observed in experiments for the corresponding load levels. The macroscopic displacement versus temperature responses are also close, as seen in Fig. 11. Upon complete heating, it can be seen that the load point displacement in numerical simulation returns to its starting value whereas the load point displacement in experiments does not. This should be attributed to TRIP strains, which are not accounted for in the simulations but can be observed in the uniaxial isobaric heating-cooling results in Fig. 1b. Crack extension with respect to the cycle number is plotted in Fig. 12, both from the experimental data and the simulation results. The crack extension per cycle from experiments was obtained by measuring the crack length at the LCT and subtracting the initial crack length. In Fig. 12 a, it can be seen that the majority of the crack extension when

 $J_0 = 2.81 \text{ KJ/m}^2$ is linear, with a nonlinearity occurring at the very end of the experiments, which corresponds to unstable crack growth and ultimate failure. For the stable crack growth regime. the average experimental crack growth rate is 0.86 mm/cycle and the average simulation crack growth is 0.6 mm/cycle, both calculated by taking the slope of the linear portion of the crack growth curve. For $J_0 = 1.25 \text{ KJ/m}^2$ (Fig. 12b), again, it can be seen that most of the crack growth per cycle is linear, with a deviation towards the end, corresponding to unstable crack growth. The average experimental crack growth rate is calculated as 0.34 mm/cycle whereas the numerical growth rate is 0.26 mm/cycle. Experimental data and simulation results match well, especially when $I_0 = 1.25 \text{ KJ/}$ m² and the crack growth data is collected over a larger number of cycles. It is important to note that if an empirical law for the crack growth rates with respect to J₀ in the austenite phase was to be calibrated, it would have been configuration dependent since the level of increase of the driving force for crack growth due to phase transformation depends on the crack geometry. Furthermore, a comparison with empirical laws for fatigue crack growth under isothermal conditions that depend on the amplitude of the driving force for crack growth would not have been possible.

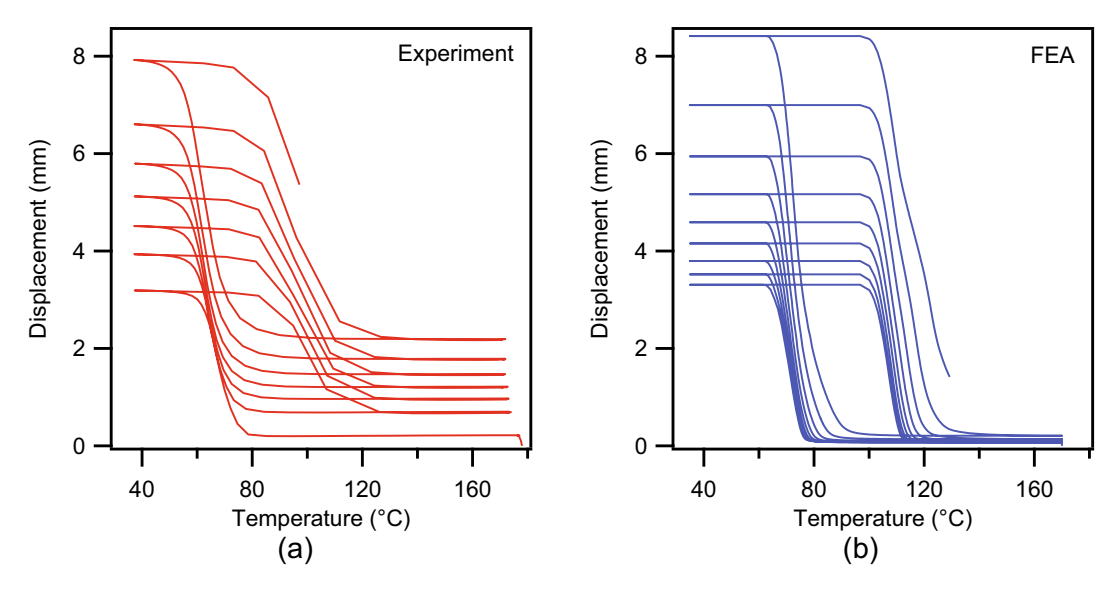


Fig. 11. Load point displacement vs. temperature for $J_0 = 2.81 \text{ kJ/m}^2$: (a) experimental measurements; (b) FEA calculations.

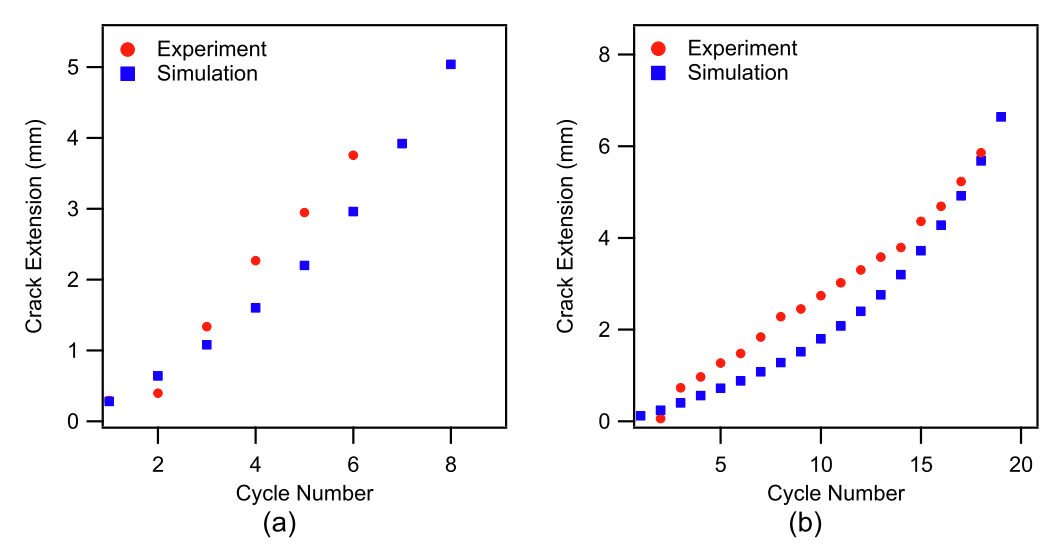


Fig. 12. Crack extension as a function of number of cycles for the NiTi CT samples that showed crack growth through multiple cycles: (a) J₀ = 2.81 KJ/m²; (b) J₀ = 1.25 KJ/m².

A notable feature of the two low-bias-load cases in both the experiments and simulations (Fig. 4) is that the final catastrophic failure occurs during heating (7th/9th and18th/20th heating cycles in the experiment and simulation, respectively) after stable crack growth proceeds through multiple cooling cycles. One possible explanation for this peculiar behavior is that the loss of beneficial shielding during heating-induced reverse phase transformation that begins behind the crack tip promotes crack growth and failure (Jape et al., 2015). As discussed previously, recovered transformation strains in the wake of the crack tip result in an antishielding effect on the crack and tend to open it. This antishielding effect results from the slight increase in the crack driving force observed during heating of infinite medium SMAs with a center crack (Jape et al., 2016a, 2016b), although the driving force for SMA CT specimen with an initial crack (Fig. 8) does not show this increase during heating. It is, however, likely that after the crack has grown substantially (by 8-9 mm, in this case), stress redistribution near the crack tip during heating leads to sudden increase in the crack driving force and subsequent anti-shielding effect causes the catastrophic failure. From an experimental point of view, other effects arising from sharp temperature gradients, material processing defects, or structural instabilities are also some likely causes for the unusual failure of the specimen. On the other hand, from a numerical perspective, a sudden increase in crack driving force beyond the specified tolerance due to stress redistribution during heating can result in numerical instabilities and failure. To properly characterize the catastrophic failure of SMAs subjected to thermomechanical loading, this phenomenon needs further attention from both experimental and simulation efforts and will be addressed in follow-up studies.

5. Summary and conclusions

In this paper, stable crack growth in SMAs, thermally cycled under a constant bias load (*i.e.*, so-called actuation loading), is observed for the first time. The observed response is multiple-cycle actuation-induced overload crack growth rather than actuation fatigue crack growth. In all experiments, the bias loads are chosen so that crack advances during the very first cooling cycle. For every thermal cycle, crack growth occurs during cooling once the sample reaches a specific temperature. Crack growth then ceases at a lower temperature and the crack remains static upon further cooling. In some experiments crack growth was also observed during heating just before failure.

Numerical simulations based on the recently measured fracture toughness of NiTi show good agreement with the experimental results and provide confidence on the insight provided in the actuation fracture response of SMAs on the basis of the constitutive model. As the material is progressively cooled, pronounced phase transformation in front of the crack tip results in elevated driving force that triggers crack advance. Stable crack growth results from the shielding effect provided by the transformed material left in the wake of the growing crack (due to the Clausius-Clapeyron relation, the material in front of the crack transforms first during cooling). Thus, phase transformation plays a dual role on the crack growth kinetics by raising the driving force for crack growth when occurring in a fan in front of the crack tip and providing a shielding effect when occurring behind this fan.

Declaration of Competing Interest

The authors declare that they have no known competing financial interests or personal relationships that could have appeared to influence the work reported in this paper.

Acknowledgements

This study was supported by the US Air Force Office of Scientific Research, under Grant no. FA9550-18-1-0276 and the NASA University Leadership Initiative Grant Number NNX17AJ96A. BY, TB, and IK also acknowledge the support from US National Science Foundation, Grant No. CMMI-1917367.

Appendix

SMA constitutive model

The phenomenological constitutive model used for the analysis in this paper captures the behavior of stabilized diffusionless solid-to-solid phase transformation in polycrystalline SMA materials (Boyd and Lagoudas, 1996; Lagoudas et al., 2012). This model is developed within the framework of continuum thermodynamics adopting a classical small-strain rate independent formulation for the evolution of transformation strains and an isotropic elastic response. The derivation of this model begins with the choice of a thermodynamic free energy potential (Gibbs free energy is chosen for this model) and complementary independent internal and external state variables (see (Lagoudas et al., 2012) for more details). Some relevant features of the constitutive model are presented here.

The incremental total strain tensor, $d\varepsilon_{ij}$, is given as follows:

$$d\varepsilon_{ij} = S_{ijkl}d_{kl} + dS_{ijkl}\sigma_{kl} + d\varepsilon_{ij}^t,$$

where σ_{ij} and ε^t_{ij} are the Cartesian components of the stress tensor and the transformation strain tensor, respectively, and S_{ijkl} are the components of the current elastic compliance tensor. The dependence of this current compliance tensor on the martensite volume fraction ξ is given as,

$$S_{ijkl} = (1 - \xi)S_{iikl}^A + \xi S_{iikl}^M,$$

where S_{ijkl}^{A} and S_{ijkl}^{M} are the components for the austenite and martensite compliance tensors. Due to the assumption of elastic anisotropy for the pure austenite and martensite phases, the expression for the individual compliance tensors can be written as,

$$S_{iikl}^{\alpha} = (1 + \nu_{\alpha})/2\nu_{\alpha} (\delta_{il}\delta_{jk} + \delta_{ik}\delta_{jl}) - (\nu_{\alpha}/E_{\alpha})\delta_{ij}\delta_{kl},$$

where α stands for A when austenite and M when martensite, E_{α} and ν_{α} are the Young's modulus and Poisson's ratio, and δ_{ij} is the Kronecker's delta. The evolution equation for the transformation strain can now be defined as a function of ξ as,

$$d\varepsilon_{ij}^t = \Lambda_{ij}d\xi$$

where $\Lambda_{ij}=\Lambda^{fwd}_{ij}$ for forward phase transformation or $d\xi>0$, and $\Lambda_{ij}=\Lambda^{rev}_{ij}$ for reverse phase transformation or $d\xi<0$. The components of the direction tensor Λ_{ij} are defined as,

$$\Lambda_{ij}^{fwd} = \frac{3}{2} H^{cur} \frac{\boldsymbol{\sigma}'}{\overline{\boldsymbol{\sigma}}}$$

$$\Lambda^{rev}_{ij} = \frac{\mathcal{E}^t_{ij}}{\mathcal{E}} s_{ij}$$

where H^{cur} is the uniaxial transformation strain magnitude at complete phase transformation, $\overline{\sigma} = \sqrt{\frac{3}{2}\sigma' : \sigma'}$ is the von Mises equivalent stress, and σ' is the deviatoric part of the stress tensor. During forward transformation, the orientation of the transformation strain is determined by the direction of the applied stress, which motivates the selected J_2 form of the direction tensor (Lagoudas et al., 2012). On the other hand, during reverse phase transformation,

the direction and magnitude of the transformation strain is governed by the average orientation of the martensite at the cessation of partial or full transformation.

Since SMAs do not exhibit a constant maximum transformation strain at all stress levels, the *current* level of the transformation strain H^{cur} can be described as a decaying exponential function dependent on the minimum transformation strain H_{min} , the ultimate transformation strain magnitude at high stress levels H_{sat} , a critical stress level $\overline{\sigma}_{crit}$, and a rate parameter k:

$$H^{cur}(\overline{\sigma}) = \begin{cases} H_{min}; & \overline{\sigma} \leq \overline{\sigma}_{crit}, \\ H_{min} + (H_{sat} - H_{min}) \Big(1 - e^{-k \left(\overline{\sigma} - \overline{\sigma}_{crit} \right)} \Big); & \overline{\sigma} > \overline{\sigma}_{crit} \end{cases}$$

During phase transformation, not unlike J_2 plasticity, the transformation surface is defined as follows:

$$\Phi = 0, \Phi = \left\{ egin{array}{l} \Phi^{ ext{fwd}} = \pi^{ ext{fwd}} - Y_0, d\xi > 0, \ \Phi^{ ext{re}
u} = -\pi^{ ext{re}
u} - Y_0, d\xi < 0, \end{array}
ight.$$

where π^{fwd} and π^{rev} are the thermodynamic driving forces for forward and reverse phase transformation, respectively, and Y_0 is the critical thermodynamic force for transformation. The driving forces during forward and reverse transformation can be written as:

$$\pi^{ extit{fwd}} = \sigma_{ij} \Lambda^{ extit{fwd}}_{ij} + rac{1}{2} \Delta S_{ijkl} \sigma_{ij} \sigma_{kl} +
ho \Delta s_0 T -
ho \Delta u_0 - f^{ extit{fwd}}$$

$$\pi^{rev} = \sigma_{ij} \Lambda^{rev}_{ij} + rac{1}{2} \Delta S_{ijkl} \sigma_{ij} \sigma_{kl} +
ho \Delta s_0 T -
ho \Delta u_0 - f^{rev}$$

where

$$f^{\text{fwd}} = \frac{1}{2}\alpha_1 \left[1 + \xi^{n_1} - (1 - \xi)^{n_2} \right] + \alpha_3$$

$$f^{rev} = \frac{1}{2}\alpha_2 [1 + \xi^{n_3} - (1 - \xi)^{n_4}] - \alpha_3$$

The functions f^{fwd} and f^{rev} describe the hardening behavior during forward and reverse phase transformation, respectively, s_0 is the specific entropy, u_0 is the specific internal energy, ρ is the density, and Δ denotes the difference in properties between martensite and austenite states, and n_1, n_2, n_3, n_4 are modeling parameters with real number values in the interval (0,1] and are determined from experimental measurements.

Given these SMA material constitutive relations, the following model parameters need to be calibrated from experimental measurements: (a) the elastic parameters of austenite and martensite (E_A, E_M, v_A, v_M) , (b) parameters for the functional form of the transformation strain $H^{cur}(k, H_{sat})$, and (c) six parameters that characterize the martensitic phase transformation $(\rho \Delta s_0, \rho \Delta u_0, \alpha_1, \alpha_2, \alpha_3, Y_0)$. This also results in the calibrated parameters: M_s , M_f , A_s , A_f being the martensite-start, martensite-finish, austenite-start, and austenite-finish transformation temperatures, respectively, and C_M , C_A being the forward and reverse transformation slopes on the stress–temperature phase diagram. Once properly calibrated, the constitutive model can then be utilized to model the behavior of SMAs under a range of thermomechanical loading conditions.

References

- Abaqus Analysis User's Manual. 2017, Dassault Systèmes of America Corp.: Woodlands Hills, CA.
- ASTM E399-17, Standard Test Method for Linear-Elastic Plane-Strain Fracture Toughness KIc of Metallic Materials. 2017, ASTM International: West Conshohocken. PA.
- ASTM E1820-13, Standard Test Method for Measurement of Fracture Toughness. 2013, ASTM International: West Conshohocken, PA.

- Atli, K., Karaman, I., Noebe, R., Garg, A., Chumlyakov, Y., Kireeva, I., 2011. Shape memory characteristics of Ti49. 5Ni25Pd25Sc0. 5 high-temperature shape memory alloy after severe plastic deformation. Acta Mater. 59 (12), 4747–4760.
- Baxevanis, T., Chemisky, Y., Lagoudas, D., 2012. Finite element analysis of the plane strain crack-tip mechanical fields in pseudoelastic shape memory alloys. Smart Mater. Struct. 21. (9) 094012.
- Baxevanis, T., Lagoudas, D., 2012. A mode I fracture analysis of a center-cracked infinite shape memory alloy plate under plane stress. Int. J. Fract. 175 (2), 151–166
- Baxevanis, T., Lagoudas, D., 2015. Fracture mechanics of shape memory alloys: review and perspectives. Int. J. Fract. 191 (1–2), 191–213.
- Baxevanis, T., Parrinello, A., Lagoudas, D., 2013. On the fracture toughness enhancement due to stress-induced phase transformation in shape memory alloys. Int. J. Plast. 50, 158–169.
- Baxevanis, T., Landis, C.M., Lagoudas, D.C., 2014. On the fracture toughness of pseudoelastic shape memory alloys. J. Appl. Mech. 81, (4) 041005.
- Baxevanis, T., Parrinello, A., Lagoudas, D., 2016. On the driving force for crack growth during thermal actuation of shape memory alloys. J. Mech. Phys. Solids 89, 255–271.
- Benafan, O., Brown, J., Calkins, F., Kumar, P., Stebner, A., Turner, T., Vaidyanathan, R., Webster, J., Young, M., 2014. Shape memory alloy actuator design: CASMART collaborative best practices and case studies. Int. J. Mech. Mater. Des. 10 (1), 1–42.
- Boyd, J.G., Lagoudas, D.C., 1996. A thermodynamical constitutive model for shape memory materials. Part I. The monolithic shape memory alloy. Int. J. Plast. 12 (6), 805–842.
- Creuziger, A., Bartol, L., Gall, K., Crone, W., 2008. Fracture in single crystal NiTi. J. Mech. Phys. Solids 56 (9), 2896–2905.
- Daly, S., Miller, A., Ravichandran, G., Bhattacharya, K., 2007. An experimental investigation of crack initiation in thin sheets of nitinol. Acta Mater. 55 (18), 6322–6330.
- Daymond, M., Young, M., Almer, J., Dunand, D., 2007. Strain and texture evolution during mechanical loading of a crack tip in martensitic shape-memory NiTi. Acta Mater. 55 (11), 3929–3942.
- El Feninat, F., Laroche, G., Fiset, M., Mantovani, D., 2002. Shape memory materials for biomedical applications. Adv. Eng. Mater. 4 (3), 91–104.
- Gall, K., Yang, N., Sehitoglu, H., Chumlyakov, Y.I., 2001. Fracture of precipitated NiTi shape memory alloys. Int. J. Fract. 109 (2), 189–207.
- Gollerthan, S., Young, M., Neuking, K., Ramamurty, U., Eggeler, G., 2009. Direct physical evidence for the back-transformation of stress-induced martensite in the vicinity of cracks in pseudoelastic NiTi shape memory alloys. Acta Mater. 57 (19), 5892–5897.
- Gollerthan, S., Young, M., Baruj, A., Frenzel, J., Schmahl, W.W., Eggeler, G., 2009. Fracture mechanics and microstructure in NiTi shape memory alloys. Acta Mater. 57 (4), 1015–1025.
- Haghgouyan, B., Shafaghi, N., Aydıner, C.C., Anlas, G., 2016. Experimental and computational investigation of the effect of phase transformation on fracture parameters of an SMA. Smart Mater. Struct. 25, (7) 075010.
- Haghgouyan, B., Jape, S., Hayrettin, C., Baxevanis, T., Karaman, I., Lagoudas, D.C., 2018. Experimental and numerical investigation of the stable crack growth regime under pseudoelastic loading in shape memory alloys. Behavior and Mechanics of Multifunctional Materials and Composites XII. International Society for Optics and Photonics.
- Haghgouyan, B., Hayrettin, C., Baxevanis, T., Karaman, I., Lagoudas, D.C., 2019. Fracture toughness of NiTi-Towards establishing standard test methods for phase transforming materials. Acta Mater. 162, 226–238.
- Hagngouyan, B., Jape, S., Baxevanis, T., Karaman, I., Lagoudas, D.C., 2019. Stable crack growth in NiTi shape memory alloys: 3D finite element modeling and experimental validation. Smart Mater. Struct. 28, (6) 064001.
- Hartl, D.J., Lagoudas, D.C., 2007. Aerospace applications of shape memory alloys. Proc. Inst. Mech. Eng., Part G: J. Aerosp. Eng. 221 (4), 535–552. Iliopoulos, A., Steuben, J., Kirk, T., Baxevanis, T., Michopoulos, J., Lagoudas, D., 2017.
- Iliopoulos, A., Steuben, J., Kirk, T., Baxevanis, T., Michopoulos, J., Lagoudas, D., 2017. Thermomechanical failure response of notched NiTi coupons. Int. J. Solids Struct. 125, 265–275.
- Irwin, G., Handbuch der Physik VI. Vol. Chapter Fracture I. 1958, Berlin, Germany: Springer Verlag.
- Iwanaga, H., Tobushi, H., Ito, H., 1988. Basic research on output power characteristics of a shape memory alloy heat engine: (twin crank heat engine). ISME Int. J. Sep. 1. Solid Mech. Strength Mater. 31 (3) 634–637.
- JSME Int. J. Ser. 1, Solid Mech., Strength Mater. 31 (3), 634–637.

 Jahadakbar, A., Nematollahi, M., Safaei, K., Bayati, P., Giri, G., Dabbaghi, H., Dean, D., Elahinia, M., 2020. Design, modeling, additive manufacturing, and polishing of stiffness-modulated porous nitinol bone fixation plates followed by thermomechanical and composition analysis. Metals 10 (1), 151.
- Jape, S., Baxevanis, T., Lagoudas, D.C., 2014. 2014. Stable crack growth during actuation in shape memory alloys. Behavior and Mechanics of Multifunctional Materials and Composites. International Society for Optics and Photonics.
- Jape, S., Parrinello, A., Baxevanis, T., Lagoudas, D.C., 2015. On the fracture response of shape memory alloy actuators. Proceedings of the TMS Middle East—Mediterranean Materials Congress on Energy and Infrastructure Systems (MEMA 2015). Springer.
- Jape, S., Solomou, A., Baxevanis, T., Lagoudas, D.C., 2016a. Fracture toughness of shape memory alloy actuators: effect of transformation-induced plasticity.
 Behavior and Mechanics of Multifunctional Materials and Composites 2016. International Society for Optics and Photonics.
- Jape, S., Baxevanis, T., Lagoudas, D., 2016b. Stable crack growth during thermal actuation of shape memory alloys. Shape Memory and Superelasticity 2 (1), 104–113

- Jape, S., Baxevanis, T., Lagoudas, D., 2018. On the fracture toughness and stable crack growth in shape memory alloy actuators in the presence of transformation-induced plasticity. Int. J. Fract. 209 (1–2), 117–130.
- Jiang, D., Bechle, N.J., Landis, C.M., Kyriakides, S., 2016. Buckling and recovery of NiTi tubes under axial compression. Int. J. Solids Struct. 80, 52–63.
- Karakalas, A.A., Machairas, T.T., Solomou, A.G., Saravanos, D.A., 2019a. Modeling of partial transformation cycles of SMAs with a modified hardening function. Smart Mater. Struct. 28, (3) 035014.
- Karakalas, A.A., Manolas, D.I., Machairas, T.T., Riziotis, V.A., Saravanos, D.A., 2019b. Active load alleviation potential of adaptive wind turbine blades using shape memory alloy actuators. Wind Energy 22 (5), 620–637.
- Karakoc, O., Hayrettin, C., Evirgen, A., Santamarta, R., Canadinc, D., Wheeler, R., Wang, S., Lagoudas, D., Karaman, I., 2019. Role of microstructure on the actuation fatigue performance of Ni-rich NiTiHf high temperature shape memory alloys. Acta Mater. 175, 107–120.
- Kockar, B., Karaman, I., Kim, J., Chumlyakov, Y., Sharp, J., Yu, C.-J.-M., 2008. Thermomechanical cyclic response of an ultrafine-grained NiTi shape memory alloy. Acta Mater. 56 (14), 3630–3646.
- Krueger, R., 2004. Virtual crack closure technique: history, approach, and applications. Appl. Mech. Rev. 57 (2), 109–143.
- Lagoudas, D.C., 2008. Shape memory alloys: modeling and engineering applications. Springer Science & Business Media.
- Lagoudas, D., Hartl, D., Chemisky, Y., Machado, L., Popov, P., 2012. Constitutive model for the numerical analysis of phase transformation in polycrystalline shape memory alloys. Int. J. Plast. 32, 155–183.
- LePage, W., 2018. Multiscale Investigation of Shape Memory. Alloy Fatigue.
- Miyazaki, S., Imai, T., Igo, Y., Otsuka, K., 1986. Effect of cyclic deformation on the pseudoelasticity characteristics of Ti-Ni alloys. Metall. Trans. A 17 (1), 115–120.
- Mohajeri, M., Case, R., Haghgouyan, B., Lagoudas, D.C., Castaneda, H., 2020. Structures, Loading influence on the corrosion assessment during stressinduced martensite reorientation in nickel-titanium SMA. Smart Mater. Struct. 29, (3) 035013.
- Nematollahi, M., Mehrabi, R., Callejas, M.A., Elahinia, H., Elahinia, M., 2018. A twoway architectural actuator using NiTi SE wire and SME spring. Active and Passive Smart Structures and Integrated Systems XII. International Society for Optics and Photonics.

- Nematollahi, M., Baghbaderani, K.S., Amerinatanzi, A., Zamanian, H., Elahinia, M., 2019. Application of NiTi in assistive and rehabilitation devices: a review. Bioengineering 6 (2), 37.
- Otsuka, K., Wayman, C.M., 1999. Shape memory materials. Cambridge university
- Robertson, S.W., Ritchie, R.O., 2007. In vitro fatigue-crack growth and fracture toughness behavior of thin-walled superelastic Nitinol tube for endovascular stents: A basis for defining the effect of crack-like defects. Biomaterials 28 (4), 700-709
- Robertson, S., Ritchie, R., 2008. A fracture-mechanics-based approach to fracture control in biomedical devices manufactured from superelastic Nitinol tube. J. Biomed. Mater. Res. B Appl. Biomater. 84 (1), 26–33.
- Rodrigues, P., Braz Fernandes, F., Paula, A., Oliveira, J., Ribeiro, S., Teixeira, E., Schell, N., 2017. Microstructural characterization of NiTi shape memory alloy produced by rotary hot forging. Powder Diffr. 32 (S1), S201–S206.
- Rybicki, E.F., Kanninen, M.F., 1977. A finite element calculation of stress intensity factors by a modified crack closure integral. Eng. Fract. Mech. 9 (4), 931–938.
- Shaw, J.A., Kyriakides, S., 1995. Thermomechanical aspects of NiTi. J. Mech. Phys. Solids 43 (8), 1243–1281.
- Stankiewicz, J., Robertson, S., Ritchie, R., 2007. Fatigue-crack growth properties of thin-walled superelastic austenitic Nitinol tube for endovascular stents. J. Biomed. Mater. Res. Part A 81 (3), 685–691.
- Vaidyanathan, R., Dunand, D., Ramamurty, U., 2000. Fatigue crack-growth in shapememory NiTi and NiTi-TiC composites. Mater. Sci. Eng., A 289 (1-2), 208-216.
- Wayman, C., Cornelis, I., Shimizu, K., 1972. Transformation behavior and the shape memory in thermally cycled TiNi. Scr. Metall. 6 (2), 115–122.
- Xu, L., Baxevanis, T., Lagoudas, D.C., 2019. A three-dimensional constitutive model for the martensitic transformation in polycrystalline shape memory alloys under large deformation. Smart Mater. Struct. 28, (7) 074004.
- Xu, L., Solomou, A., Baxevanis, T., Lagoudas, D.C., 2021. Finite strain constitutive modeling for shape memory alloys considering transformation-induced plasticity and two-way shape memory effect. Int. J. Solids Struct. 221, 42–59.
- Young, B., Haghgouyan, B., Lagoudas, D., Karaman, I., 2019. Effect of Temperature on the Fracture Toughness of a NiTiHf High Temperature Shape Memory Alloy. Shape Memory Superelasticity 5 (4), 362–373.